

A Standalone System for Resistive Smart Sensors Based on a Wheatstone Quarter-Bridge

Matei SERBANESCU¹, Vlad-Mihai PLACINTA², Florin NASTASE³,
Gheorghe PRISTAVU¹, Octavian BUIU⁴, Gheorghe BREZEANU¹, and
Bogdan SERBAN⁴

¹University *Politehnica* of Bucharest, Faculty of Electronics, Telecommunications and Information
Technology, Bucharest, Romania

²Horia Hulubei National Institute for R&D in Physics and Nuclear Engineering, Bucharest - Magurele,
Romania

³Termobit Prod, Bucharest, Romania

⁴National Institute for R&D in Microtechnologies, Bucharest, Romania

E-mails: matei.serbanescu@stud.etti.upb.ro,
vlad-mihai.placinta@nipne.ro, florin.nastase@outlook.com,
gheorghe.pristavu@upb.ro, octavian.buiu@imt.ro,
gheorghe.brezeanu@dce.pub.ro, bogdan.serban@imt.ro

Abstract. This paper presents the architecture of a resistive smart-sensor based on a Wheatstone quarter-bridge. The overall system also comprises a signal-conditioning circuit and a microcontroller. The intended sensing element is a small-variation chemo-resistive sensor. Its resistance gradient is converted by the conditioning circuit into a signal with variable duty-cycle. The proposed architecture is theoretically analyzed and validated by both simulations and measurements on a prototype, implemented with discrete and low-cost components. The output signal exhibits a maximum of 1.8% relative error, for a sensing element value variation of 10Ω . Sensing linearity is assessed via R^2 at up to 0.9995, while sensitivity reaches $57.71 \mu s/\Omega$.

Key-words: Resistive sensor, quarter-bridge, signal-conditioning circuit, microcontroller, duty-cycle.

1. Introduction

The demand for resistive sensors has grown over the years as their utility in applications like temperature, humidity, gas sensing, strain gauging, light or pressure detection increased. Their success has been driven mainly by their availability and simplicity, thus enabling the design of

low-cost and versatile interface circuits [1]. Depending on their resistance variation intervals, these types of sensors are categorized into two groups: small-resistance range (up to tens of Ω), such as temperature or humidity sensors and large-resistance range (upwards of $M\Omega$), for gas chemo-resistive sensors or soil moisture ones. For the first group, the most common readout approaches rely either on voltage dividers or Wheatstone bridge configurations [2]. For the latter option, precise matching of the bridge components leads to a better power supply ripple rejection and mitigates any other parasitic effects. Fully-linear output is achieved only for full-bridge symmetric configurations [3]. However, quarter-bridge based solutions may also deliver satisfactory quasi-linear response if the resistive sensing element exhibits small variation. In this case, the preferred conditioning circuits convert this variation into a signal of proportional period or duty-cycle. Therefore, quasi-digital converters became attractive for various applications, due to their time-variant output that could be easily acquired by digital systems like microcontrollers or SoCs/FPGAs [4–14].

Recent advances in the field of microelectronics, as well as miniaturized wireless communication solutions led to the incorporation of the sensing element, readout circuit, data processing and transmission block into a single embedded system – smart sensor. These solutions are widely used in medical, automotive, consumer or industrial applications. For instance, the use of portable or wearable systems, operating close to or directly on the human body, has enabled significant developments in the medical treatment area and shaped the smart-sensing industry over the last years. Body Sensor Networks emerged as an important field of research and development meant to support new therapeutic methodologies and real-time decision making, based on continuous and non-invasive monitoring [15–19]. Essentially, smart-sensing systems provide cost-reduction in patient care, while enabling early diagnosis of different medical conditions, hence improving quality of life. Currently, the main challenges in the smart-sensing field are obtaining simple, low-cost signal-conditioning solutions, which are both scalable and energy efficient.

This paper proposes a smart-sensor architecture, suitable for small-resistance-variation sensors, using the Wheatstone quarter-bridge configuration. The intended sensing element is a chemo-resistive sensor [20]. To validate this approach, a prototype was implemented on a printed circuit board (PCB) and its performances were evaluated. The goal was to obtain a strong linear dependence between the output of the signal-conditioning block and the sensor response.

Section 2 presents the proposed system topology and discusses the operation principles. Simulation and experimental results, focused on transient response and transfer characteristics are given and interpreted in Section 3. Conclusions and future work considerations are discussed in Section 4.

2. Smart-sensing architecture

The block diagram of the proposed architecture is depicted in Fig. 1. It comprises a Wheatstone quarter-bridge, a signal-conditioning block and a microcontroller. The Sensor (Fig. 1) can be modeled as a variable resistor with a baseline value of $R_S \cong 51 \Omega$ [20]. In order to balance the bridge, the other resistors are also set at R_S . Thus, the differential output voltage ($V_X - V_Y$) as a function of supply voltage (V_{DD}) and sensor variation (ΔR_S) is:

$$V_X - V_Y = \frac{V_{DD}}{2} \cdot \frac{\Delta R_S}{2 \cdot R_S + \Delta R_S} \quad (1)$$

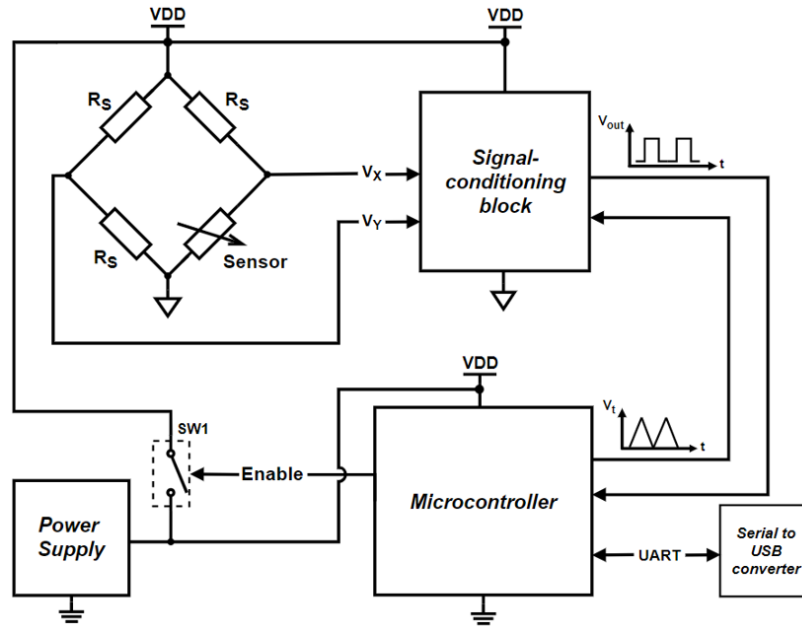


Fig. 1. The proposed smart-sensor architecture.

Figure 2 shows a detailed implementation of the signal-conditioning block. This topology, appropriate for small-resistance-variation sensing elements, is meant to produce an output signal with a duty-cycle proportional to the change in the sensing element resistance. Unity gain amplifiers, U1 and U2, serve to avoid any pre-existing loading on the diagonal nodes of the bridge.

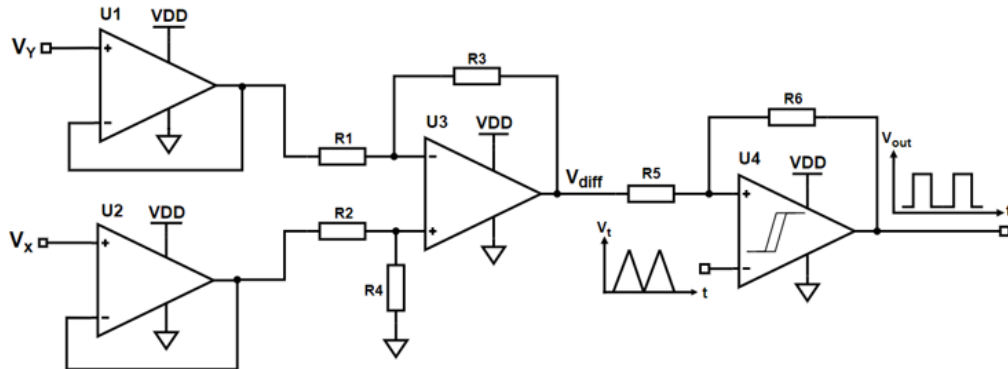


Fig. 2. Signal-conditioning circuit schematic [14].

A key element of the proposed signal-conditioning circuit is the differential voltage amplifier ($R_1 - R_4$ and U3 – Fig. 2). It suitably magnifies the bridge output voltage ($V_X - V_Y$) and alleviates the errors induced by the U1, U2 (Fig. 2) offset voltages and the tolerances of the bridge resistors (R_S – Fig. 1). The differential voltage amplifier's output, V_{diff} , is discriminated, via comparator U4 (with hysteresis added by R_5 and R_6 – Fig. 2) against a triangle signal (V_i),

generated by the microcontroller (Fig. 1). This yields a duty-cycle modulated output that depends on the sensing element variation (ΔR_S). For simplicity reasons, it was considered that $R_1 = R_2$ and $R_3 = R_4$. Therefore, the gain (A_d) of the differential amplifier is given by the ratio between R_3 and R_1 . V_{diff} is calculated as:

$$V_{diff} = A_d \cdot (V_X - V_Y) = \frac{R_3}{R_1} \cdot (V_X - V_Y) \quad (2)$$

The output of U4 will be "High" when $V_{diff} > V_t$ and "Low" when $V_{diff} < V_t$. The corresponding ON and OFF times are determined, with respect to the period (T) of the triangle signal, as in [14]:

$$T_{ON} = T \cdot \frac{V_{diff}}{V_t} \quad (3)$$

$$T_{OFF} = T \cdot \left(1 - \frac{V_{diff}}{V_t}\right) \quad (4)$$

The output signal (V_{out} – Fig. 2) has the same frequency as V_t and an amplitude equal to the positive supply of U4 (VDD – Fig. 2). Finally, using (1) - (4), T_{ON} can be expressed, as a function of the sensor's variation (ΔR_S), thus:

$$T_{ON} = k \cdot \frac{\Delta R_S}{2 \cdot R_S + \Delta R_S} \quad (5)$$

$$k = \frac{A_d \cdot VDD \cdot T}{2 \cdot V_t} \quad (6)$$

In (5), k is the main factor which determines the sensitivity of the conditioning circuit (Fig. 2). Increasing its value can be primarily achieved by tuning the values of A_d and T, as adjusting VDD or V_t will either significantly increase power consumption or cause control loop instability. The gain of the differential amplifier determines the lowest detectable ΔR_S step. However, its value should not lead to V_{diff} (eq. (2)) exceeding the comparator's (U4 – Fig. 2) maximum common-mode input voltage.

The microcontroller (Fig. 1) must possess a few important features. First of all, it should have at least two input capture modules (IC) for the acquisition of the comparator output signal (V_{out} – Fig. 1). In order to generate the triangle signal (V_t – Fig. 1), it should include either a Digital-to-Analog Converter (DAC) or a dedicated Slope Generator (SG). Using a DAC can sensibly degrade signal fidelity for high period values (T), which will lead to parasitic transitions at the output of the comparator. This issue can be mitigated by the much finer discretization step of the SG.

From a practical standpoint, the microcontroller is powered by the same supply (VDD) as the rest of the blocks in Fig. 1. An integrated solution (Power Supply – Fig. 1) delivers this voltage, while a switch (SW1 – Fig. 1) was included in order to offer additional power management options. The debugging and data transmission interface to a computer was ensured by a Serial to USB converter (Fig. 1).

3. Results and performances

The system functionality was initially validated via simulations, using the Multisim software tool from National Instruments. For U1, U2 and U3 (Fig. 2), the OPA317 [21] model was selected due to its small input offset voltage (*i.e.*, typical $20 \mu\text{V}$), extremely low input bias currents (*i.e.*, typical 155 pA) and rail-to-rail input/output operation. Moreover, it has the possibility to work at supply voltages between 1.8 V and 5.5 V . Comparator U4 (Fig. 2) was implemented using LMV761 [22], a precision comparator with push-pull output stage and shutdown function, used to disable the circuit and to reduce the supply current. The three operational amplifiers, U1-3, and the comparator, U4, were all powered by an ideal 3.3 V supply. The three fixed bridge resistors (R_S – Fig. 1) were set to 51Ω [20]. In order to emulate the behavior of the chemoresistive sensing element, the variable bridge resistor (Sensor – Fig. 1) was incremented in the $51.4 \Omega - 61 \Omega$ range, with a step of 0.4Ω . $R_1 = R_2 = 10 \text{ k}\Omega$ and $R_3 = R_4 = 100 \text{ k}\Omega$ were selected, which led to a gain of 10 for the differential amplifier. The triangle signal (V_t – Fig. 2) was considered ideal, with a period of 1 ms and 2.5 V amplitude.

Figure 3 illustrates simulations for Sensor values ($R_S + \Delta R_S$) of 59Ω and 59.4Ω , respectively, presenting the waveforms of the main readout nodes (Fig. 2).

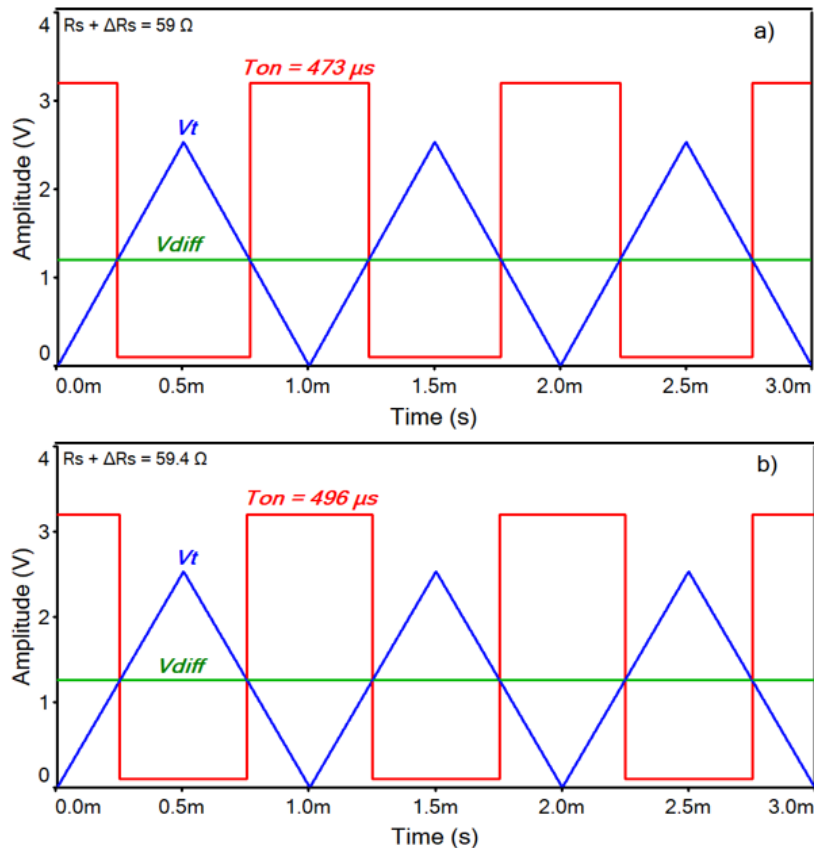


Fig. 3. Waveforms of the main circuit nodes for Sensor values of: a) 59Ω and b) 59.4Ω .

It can be observed that a 0.4Ω increase in ΔR_S determines a $23 \mu\text{s}$ larger T_{ON} . This resolution is essential to ensure that the microcontroller can accurately detect even minute shifts in sensor resistivity.

A PCB prototype of the smart-sensing system was implemented with discrete components. Their selection was done considering the following: package area, cost, single-supply operation and availability. Therefore, for the signal-conditioning circuit (Fig. 2), components corresponding to the models used in simulations were employed: OPA4317 for U1-3 and LMV761 for U4. The supply voltage (VDD – Fig. 1) is delivered by an integrated, synchronous buck regulator, MCP1603 from Microchip [23], that features a wide input range ($2.7 \text{ V} - 5.5 \text{ V}$) and a fixed output voltage (3.3 V). The chosen microcontroller (Fig. 1) was a 16-bit, 28-pin, dsPIC33CK256 [24] from Microchip, embedding both IC and DAC modules, as well as multiple communication interfaces.

Figure 4 depicts the $6 \text{ cm} \times 4 \text{ cm}$, double-sided PCB. The chemo-resistive sensing element's (Sensor – Fig. 1) variation was modeled by an ensemble of a 51Ω resistor connected in series with a 10Ω , 25 turns, 3296 Series trimmer, from Bourns [25]. The rest of the Wheatstone bridge was populated with similar 51Ω resistors (R_S – Fig. 1). $R_1 = R_2 = 10 \text{ k}\Omega$ and $R_3 = R_4 = 100 \text{ k}\Omega$ were placed.

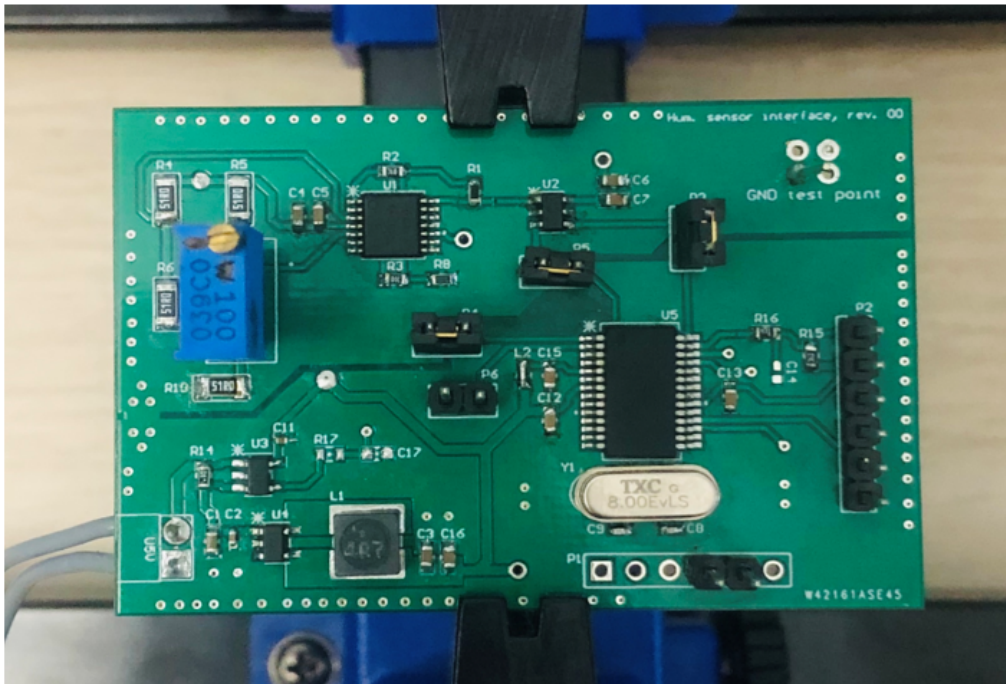


Fig. 4. PCB prototype of the proposed architecture.

Resistors R_5 and R_6 were selected at $1 \text{ k}\Omega$ and $100 \text{ k}\Omega$ respectively. This created a 33 mV hysteresis for the comparator. All fixed resistors have 1% tolerance ratings. The power supply pins for U1-4 (Fig. 2) and microcontroller (Fig. 1) were decoupled with parallel groups of $0.1 \mu\text{F}$ and $10 \mu\text{F}$ low-ESR ceramic capacitors to suppress noise-induced effects.

In order to demonstrate the smart sensor's response linearity, the dependence between T_{ON} and ΔR_S was established for Sensor (Fig. 1) resistive variations between 51.4Ω and 61Ω , with a step of 0.4Ω , matching the simulations. For each trimmer turn, the equivalent ΔR_S value was precisely determined using a GDM8341 GW Instek multimeter, before acquiring T_{ON} . The experimental setup was completed with an external DC Power Supply - E3642, that delivered the 5 V system input voltage and a digital oscilloscope - DSOX1204, both from Keysight Technologies.

An oscilloscope capture, depicting the prototype operation, is shown in Fig. 5. The amplitude and frequency of the triangle signal (V_t – Fig. 1) and the comparator output signal (V_{out} – Fig. 1) can be observed. Next, Fig. 6 presents the rise and fall edges of U4 output, proving that no parasitic transitions occur, as a direct result of introducing the hysteresis window.

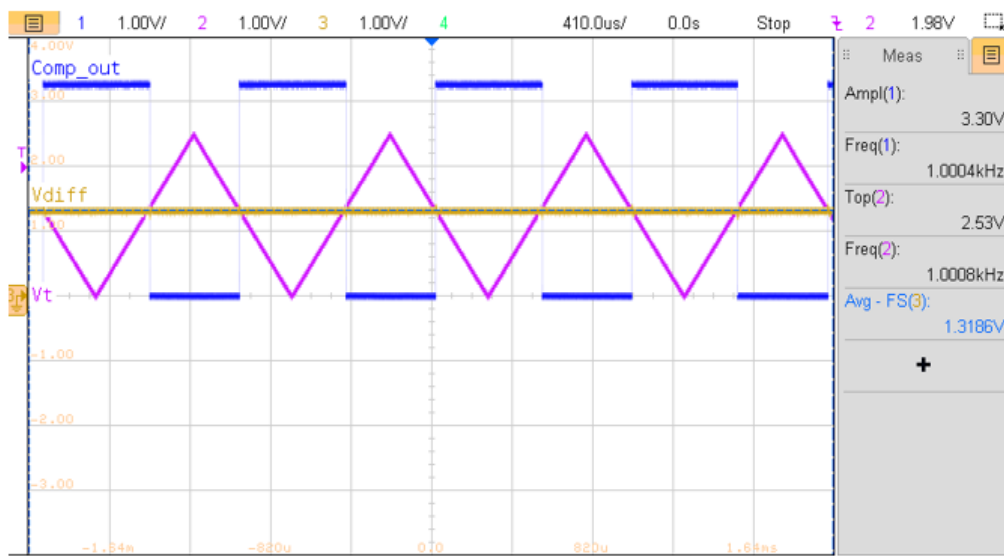


Fig. 5. Oscilloscope capture for $R_S + \Delta R_S = 59.8 \Omega$.

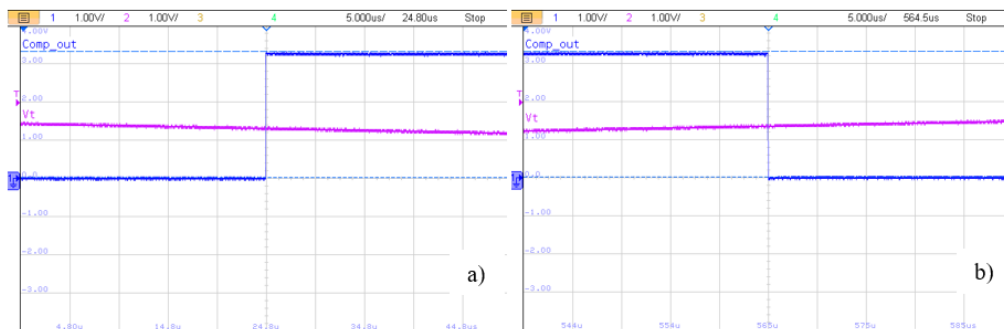


Fig. 6. a) Rise and b) fall edges of the comparator's output signal.

As pointed out in Section 2, the microcontroller in Fig. 1 is responsible for generating the triangle signal (V_t – Fig. 1), acquiring the comparator output voltage (V_{out} – Fig. 1) and sending out the data to a computer via the UART protocol. The triangle waveform is conventionally obtained by sending samples to the DAC, possibly using a Direct Memory Access module. However, this method requires periodic CPU intervention to trigger transfers and compute samples. Therefore, the microcontroller’s dedicated Slope Generator was used, which does not strain the CPU. It can generate triangle waveforms with preset, paired values for frequency and amplitude [24]. The best suited combo for the proposed smart-sensing application was 1 kHz frequency, at 2.5 V amplitude. Higher frequencies would entail V_t amplitudes below experimental V_{diff} values, breaking the control loop.

Measuring the T_{ON} time of the comparator’s output was performed with minimal CPU loading. Usually, a single IC module would be necessary. This kind of module has a free running timer and whenever an event occurs, the timer value is stored separately. In this work, the events of interest were the rising and falling edges of the comparator’s output signal (V_{out}). However, in the case of very short T_{ON} pulses (\sim microseconds) the interrupt routine might not be serviced fast enough, determining the microcontroller to batch several V_{out} periods into a single computation cycle. In order to eliminate this issue, two independent IC modules were employed, one for the rising edge and the other one for the falling edge, as shown in Fig. 7.

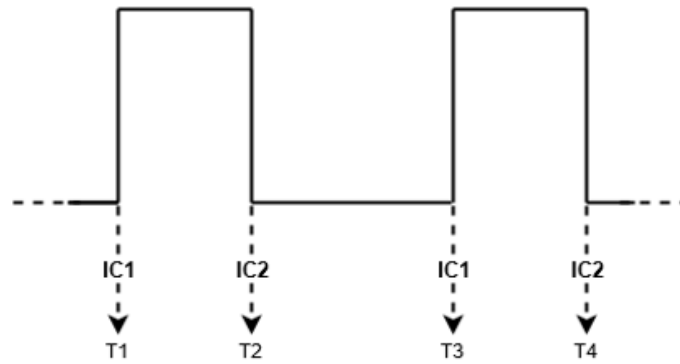


Fig. 7. T_{ON} measurement using two IC modules.

When the first rising edge appears, IC1 module saves the timer value T1. Then, IC2 saves the equivalent T2 value, for the falling edge. The pulse duration, in seconds, can be computed using:

$$T_{ON} = (T2 - T1) \cdot \text{timer period} \tag{7}$$

The same calculation is done on the next pulse, yielding the T3 and T4 values (Fig. 7). The T_{ON} durations were computed by the microcontroller for each of the 25 measured points, corresponding to the 51.4 Ω - 61 Ω Sensor variation range. The data was sent to a computer via UART protocol.

Thus, the experimental transfer characteristic of the smart-sensor is illustrated, alongside its theoretical and simulated counterparts, in Fig. 8.

A strong system linearity, corroborated by a coefficient of determination (R_{lin}^2) of 0.9995, was demonstrated from a linear fit on the experimental curve (Fig. 8). The interface sensitivity was determined to be 57.71 $\mu\text{s}/\Omega$.

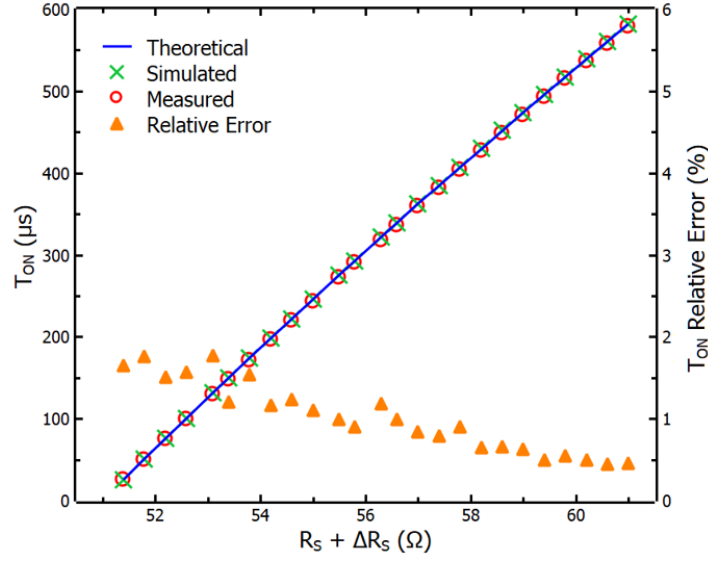


Fig. 8. T_{ON} as a function of the sensor's resistive variation: theoretical values (blue line) based on (5), simulated values (green crosses), measured values (red circles) and relative error (orange triangles).

Additionally, a coefficient of determination was also calculated as a statistical indicator of how well the theoretical model (eq. (5)) replicates the measured data:

$$R_{th}^2 = 1 - \frac{\sum_i (m_i - t_i)^2}{\sum_i (m_i - \bar{m})^2} \quad (8)$$

where m_i are the measured points, with an average of \bar{m} and t_i is the theoretical value associated with m_i . An $R_{th}^2 = 0.9997$ was obtained, which indicates excellent agreement between experimental results and calculations, also corroborated by the maximum relative error, of only 1.8%. Minor discrepancies occur because of the operational amplifiers' input offset (U1-3 – Fig. 2), supply voltage variations (e.g., VDD has a measured mean value of 3.295 V and a ripple value of 13 mV_{pp}) and the potential mismatches of the R_S resistors in the bridge.

So far, simulations and measurements were carried out only for an input resistive range corresponding to [20]. However, we plan to extend the study and test this approach to other types of resistive sensors, such as low strain piezoresistive [26] and ethanol sensors [27].

4. Conclusions

This paper presented a smart-sensing architecture suitable for resistive sensors with small variations based on a Wheatstone quarter-bridge. The proposed solution constitutes a simple and robust approach, with a reduced number of components, relying mainly on two unity gain amplifiers, a differential amplifier, a comparator plus a microcontroller facilitating digital processing and data transmission. Models for these components were chosen based on a favorable compromise between performance, cost and integration possibilities. The circuit concept was

theoretically demonstrated and its functionality was subsequently validated in simulations and experimentally. As sensing element, a chemo-resistive sensor with low output resistance variation over the full range (less than 10 ohms) was considered.

Results showed excellent linearity ($R_{lin}^2 = 0.9995$) of the system's transfer characteristic, with very good agreement between calculated and experimental data ($R_{th}^2 = 0.9997$). The relative error, under 2%, was mainly caused by the operational amplifiers' offset, bridge mismatches and voltage supply variations.

Further work includes defining a calibration algorithm, adding a wireless data-transfer solution as well as exploring battery supply operation.

Acknowledgements. This work has been funded by the Operational Program Human Capital of the Ministry of European Funds through the Financial Agreement: 51675/09.07.2019, SMIS code 125125.

References

- [1] FLAMINNI A., DEPARI A., *Advanced interfaces for resistive sensors*, Smart Sensors and MEMS, 2018, pp. 171–219.
- [2] GOMEZ-RAMIREZ E. *et al.*, *A highly robust interface circuit for resistive sensors*, Electronics, 2019 **8**, 263.
- [3] DE GRAAF G., WOLFFENBUTTEL R. F., *Systematic Approach for the Linearization and Readout of Nonsymmetric Impedance Bridges*, IEEE Transactions on Instrumentation and Measurement, 2006 **55**(5), pp. 1566–1572.
- [4] DE MARCELLIS A., FERRI G., MANTENUTO P., *Analog Wheatstone bridge-based automatic interface for grounded and floating wide range resistive sensors*, Sensors and Actuators B: Chemical, 2013 **187**, pp. 371–378.
- [5] PONNALAGU R. N., GEORGE B., KUMAR V. J., *An improved direct digital converter for bridge connected resistive sensors*, IEEE Sensors Journal, 2016 **16**(10), pp. 3679–3688.
- [6] DEPARI A. *et al.*, *A new and fast-readout interface for resistive chemical sensors*, IEEE Transactions on Instrumentation and Measurement, 2010 **59**(5).
- [7] PONNALAGU R. N., GEORGE B., KUMAR V. J., *A linearizing digitizer for Wheatstone bridge based signal conditional of resistive sensors*, IEEE Sensors Journal, 2017 **17**(6), pp. 1696–1705.
- [8] REZVANITABAR A. *et al.*, *A Power-Efficient Bridge Readout Circuit for Implantable, Wearable, and IoT Applications*, IEEE Sensors Journal, 2020 **20**(17), pp. 9955–9962.
- [9] HIDALGO-LOPEZ J. A. *et al.*, *Fast calibration methods for resistive sensor readout based on direct interface circuits*, Sensors, 2019 **19**, 3871.
- [10] ALVAREZ-SIMON L. C., GOMEZ-RAMIREZ E., SANZ-PASCUAL M. T., *Low-power highly robust resistance-to-period converter*, Sensors, 2019 **19**(8).
- [11] DE MARCELLIS A., FERRI G., MANTENUTO P., *A novel 6-decades fully-analog uncalibrated Wheatstone bridge-based resistive sensor interface*, Sensors and Actuators B: Chemical, 2013 **189**, pp. 130–140.
- [12] DEPARI A. *et al.*, *Fast, Versatile, and Low-Cost Interface Circuit for Electrochemical and Resistive Gas Sensor*, IEEE Sensors Journal, 2014 **14**(2), pp. 315–323.
- [13] HAN K. *et al.*, *A 24.88 nV/Hz Wheatstone Bridge Readout Integrated Circuit with Chopper-Stabilized Multipath Operational Amplifier*, Applied Sciences, 2020 **10**, 399.

- [14] SERBANESCU M. *et al.*, *Smart-Sensing Interface for Chemo-Resistive Sensor Based on a Wheatstone Quarter-Bridge*, in Proceedings of the International Semiconductor Conference (CAS), Sinaia, Romania, 2020, pp. 77–80.
- [15] NARANJO-HERNANDEZ D., REINA-TOSINA J., ROA L.M., *Special Issue Body Sensors Networks for E-Health Applications*, *Sensors*, 2020 **20**, 3944.
- [16] STAVROPOULOS T.G. *et al.*, *IoT Wearable Sensors and Devices in Elderly Care: A Literature Review*, *Sensors*, 2020 **20**, 2826.
- [17] PARK Y.-G., LEE S., PARK J.-U., *Recent Progress in Wireless Sensors for Wearable Electronics*, *Sensors*, 2019 **19**, 4353.
- [18] SHU L. *et al.*, *A review of emotion recognition using physiological signals*, *Sensors*, 2018 **18**, 2074.
- [19] HAYATLEH K. *et al.*, *A high performance skin impedance measurement circuit for biomedical applications*, *Journal of Circuits, Systems and Computers*, 2019 28(7).
- [20] SERBAN B.-C. *et al.*, *Oxidized carbon Nanohorns as novel sensing layer for resistive humidity sensor*, *Acta Chim. Slov.*, 2020 **67**, pp. 469–475.
- [21] Texas Instruments, *OPAx317 Zer-Drift, Low-Offset, Rail-to-Rail I/O Operational Amplifier Precision Catalog*, OPA4317 datasheet, May 2013 [Revised June 2016].
- [22] Texas Instruments, *LMV76x and LMV762Q-Q1 Low-Voltage, Precision Comparator With Push-Pull Output*, LMV761 datasheet, February 2002 [Revised October 2015].
- [23] Microchip, *2.0 MHz, 500 mA Synchronous Buck Regulator*, MCP1603 datasheet, 2007-2012.
- [24] Microchip, *dsPIC33CK256MP FAMILY, dsPIC33CK256MP502* datasheet, 2017-2020.
- [25] Bourns, *3296 - 3/8 Square Trimpot Trimming Potentiometer, 3296W-1-100* datasheet, March 2015 [Revised August 2019].
- [26] SIMIONESCU O. *et al.*, *Nanocrystalline graphite thin layers for low-strain, high-sensitivity piezoresistive sensing*, *Reviews on Advanced Materials Science*, 2020, **59**(1), pp. 306–313.
- [27] COBIANU C. *et al.*, *OrganicInorganic Ternary Nanohybrids of Single-Walled Carbon Nanohorns for Room Temperature Chemiresistive Ethanol Detection*, *Nanomaterials*, 2020 **10**, 2552.